

## Article

# Smoothed Particle Hydrodynamics-Based Study of 3D Confined Microflows

Efstathios Chatzoglou <sup>1</sup>, Antonios Liakopoulos <sup>1,\*</sup> and Filippos Sofos <sup>2</sup>

<sup>1</sup> Hydromechanics and Environmental Engineering Laboratory, Department of Civil Engineering, University of Thessaly, Pedion Areos, 38334 Volos, Greece; efchatzoglou@uth.gr

<sup>2</sup> Condensed Matter Physics Laboratory, Department of Physics, University of Thessaly, 35100 Lamia, Greece; fsofos@uth.gr

\* Correspondence: aliakop@uth.gr

**Abstract:** In this study, we investigate the performance of the smoothed particle hydrodynamics (SPH) method regarding the computation of confined flows in microchannels. Modeling and numerical simulation with SPH involve the representation of flowing matter as distinct mass points, leading to particle discretization of the Navier–Stokes equations. The computational methodology exhibits similarities with other well-established particle methods, such as molecular dynamics (MD), dissipative particle dynamics (DPD), and smooth dissipative particle dynamics (SDPD). SPH has been extensively tested in the simulation of free-surface flows. However, studies on the performance of the method in internal flow computations are limited. In this work, we study flows in microchannels of variable cross-sections with a weakly compressible SPH formulation. After preliminary studies of flows in straight constant cross-section ducts, we focus on channels with sudden expansion and/or contraction. Flow models based on periodic or various inlet/outlet boundary conditions and their implementations are discussed in the context of 2D and 3D simulations. Numerical experiments are conducted to evaluate the accuracy of the method in terms of flowrate, velocity profiles, and wall shear stress. The relation between  $f$  and  $Re$  for constant cross-section channels is computed with excellent accuracy. SPH captured the flow characteristics and achieved very good accuracy. Compressibility effects due to the weakly compressible smoothed particle hydrodynamics (WCSPH) formulation are negligible for the flows considered. Several typical difficulties and pitfalls in the application of the SPH method in closed conduits are highlighted as well as some of the immediate needs for the method's improvement.

**Keywords:** microflows; confined flows; smoothed particle hydrodynamics (SPH); three-dimensional flow; sudden expansion/contraction



**Citation:** Chatzoglou, E.; Liakopoulos, A.; Sofos, F. Smoothed Particle Hydrodynamics-Based Study of 3D Confined Microflows. *Fluids* **2023**, *8*, 137. <https://doi.org/10.3390/fluids8050137>

Academic Editor: D. Andrew S. Rees

Received: 14 March 2023

Revised: 6 April 2023

Accepted: 20 April 2023

Published: 22 April 2023



**Copyright:** © 2023 by the authors. Licensee MDPI, Basel, Switzerland. This article is an open access article distributed under the terms and conditions of the Creative Commons Attribution (CC BY) license (<https://creativecommons.org/licenses/by/4.0/>).

## 1. Introduction

Fluid flow numerical simulation has gained wide acceptance in various industrial applications over the last decades. Conventional methods have faced insurmountable difficulties in some cases where the fluid flow involves geometrical complexities, chemical reactions, and scale problems, to mention a few [1,2]. Therefore, the use of novel numerical tools, which have been validated and proven reliable, may provide satisfactory solutions in many industrial problems, such as chemical analysis, biomedical devices, and microscopic interactions [3]. In addition, developments in microelectromechanical systems (MEMS) make it possible to fabricate very small devices [4]. Thus, the need for better evaluation of flow in such systems is of great practical importance.

Numerical methods are broadly classified into Lagrangian, Eulerian, and mixed-type Lagrangian–Eulerian methods. In the nonadaptive Eulerian approach, a fixed Cartesian mesh covers the computational domain, no remeshing is performed, and large deformations of the continuum are resolved, possibly without mesh adaptation. In adaptive Eulerian

methods, the mesh adapts to the solution and allows the computation of rather challenging flow fields. However, adaptive Eulerian methods may have limitations in terms of cost and convergence to the correct solution. In the Lagrangian approach, the mesh (when used) moves naturally and follows the boundaries, leading to a simplified numerical handling of free surfaces and interfaces, since no grid points are needed outside the continuum. Yet, large deformation of the continuum may negatively affect numerical accuracy [5]. To account for this issue, various adaptive Lagrangian methods have been proposed.

Smoothed particle hydrodynamics (SPH) is a mesh-free method, based on the concept of describing the flow by following the motion of fluid particles (point masses). The information contained in a mathematical model of a continuum medium in motion, usually a set of partial differential equations, is passed to several neighboring particles within a prescribed range [6]. The particles serve as “nodes” for the computation of any field variable, based on a built-in approximation utilizing a kernel function [7,8]. A number of SPH formulations have been proposed, covering the whole spectrum between the original Lagrangian formulation and recent Eulerian variants [9,10]. Similarities can be found in other particle methods, such as molecular dynamics (MD) [11], dissipative particle dynamics (DPD) [12], smooth dissipative particle dynamics (SDPD) [13], while hybrid or multiscale methods have been also proposed [14,15]. However, SPH is a numerical approximation of the partial differential equations of continuum mechanics, and MD, DPD, and SDPD may be implemented in flows where the continuum theory may or may not break down [16,17].

The mass conservation law should be satisfied for all cases in particle flows. Notwithstanding the fact that this is a minor problem in low Re flows, care has to be taken in violent, turbulent open-channel flows. In terms of particle methods applied to internal flows, this means that no fluid particles escape the walls. To account for particle penetration through the solid boundaries under no-slip and partial slip conditions, a boundary volume fraction wall approach along with a transport velocity method have been embedded in the SPH formulation, suggesting an accurate method that allows for accurate modeling of fixed and moving boundaries [18]. Issues related to the volume nonconservation and the nonphysical gap considered at the free surface are anticipated when introducing of a corrective cohesion force, which accounts for the proper characterization of the interaction region between a particle under study and its neighboring particles. This is implemented in the framework of weakly compressible SPH (WCSPH), aided by particle shifting techniques (PSTs) [19] and the WCSPH form with density diffusion term (named  $\delta$ -SPH) in its original iteration [20] or the recently introduced improved accuracy method [21].

Another computational challenge that SPH-oriented research has recently been facing is the treatment of viscosity, which is closely connected to the investigation of turbulent flows. For the simulated cases studied in this work, which are characterized by low Re numbers, this is not a problem, since the turbulence is not activated. An artificial viscosity term has been proposed by Monaghan [22] to improve computational efficiency. However, the real viscosity term has also been introduced, providing a better connection to real physics [23]. A comparison of existing viscosity models [24] concludes that the correction-based scheme on the irregular distribution of neighboring points around the particle under consideration performs better in terms of accuracy [25]. Emphasis has also been placed on the treatment of fluid/solid interaction boundaries. In this region, decreased accuracy has been observed due to the truncation of the integration domain. Suggested solutions include treatment of the boundary as virtual particles, similar to the Lennard–Jones methods in MD [22], ghost [26], or dummy [27] particles, and, recently, the combination of dummy particles and the normal flux method [28].

In this work, we focused on the application of SPH on low Reynolds number flows, in closed microchannels characterized by the presence of abrupt changes in cross-section area, given that there are not many published results in the literature. Open questions on such flows include the treatment of boundary conditions, the viscosity models exploited, and the accuracy of 2D and 3D geometries, among others. Turbulence modelling is another

major issue. Simulations are run using DualSPHysics code, which is implemented in C++ and CUDA languages, providing the advantage of high-performance computing (HPC) and, thus, simulating millions of particles with either CPUs or GPUs. The parallelization achieved saves computational time, which is a major issue in real-life engineering simulations [29]. Integration in time is performed with either Verlet’s or Symplectic method. Results have shown very good accuracy in terms of comparison with analytical solutions in terms of flowrate, velocity profiles, and friction factor. However, further study is necessary in order to resolve convergence issues close to the fluid/solid interface and to improve the accuracy in the imposition of BCs.

**2. Materials and Methods**

In the weakly compressible SPH formulation, the partial differential equations (PDEs) of the continuity equation and momentum equation are written in the form

$$\frac{d\rho}{dt} = -\rho \nabla \cdot v \tag{1}$$

$$\frac{dv}{dt} = -\frac{1}{\rho} \nabla P + g + \Gamma \tag{2}$$

In Equations (1) and (2), P is pressure,  $\rho$  refers to density,  $g$  represents external forces, and  $\Gamma$  stands for the dissipative terms in the momentum equation.

*2.1. Function Approximation in SPH*

The fluid is divided into a set of discrete moving particles. The method interpolates the set of the field variables by means of a kernel smoothing function,  $W$ . For function  $f(r)$ , we write

$$f(r_i) = \sum_j m_j \frac{f_j}{\rho_j} W(r_i - r_j) \tag{3}$$

The sum in Equation (3) theoretically extends over all the fluid particles, yet only particles for which  $r_i - r_j < h$  need to be considered for appropriately selected kernel function of compact support. This saves computational cost but can lead to inaccuracies close to the boundaries (especially at the wall/fluid interface).

*2.2. Weakly Compressible SPH Approximation Equations*

Introducing the SPH approximations, the governing equations are written (in indicial notation) as

$$\frac{d\rho_i}{dt} = \rho_i \sum_j \frac{m_j}{\rho_j} v_{ij} \cdot \nabla_i W_{ij} \tag{4}$$

$$\frac{dv_i}{dt} = -\sum_j m_j \left( \frac{P_j + P_i}{\rho_j \rho_i} \right) \nabla_i W_{ij} + g + \sum_j m_j \left( \frac{4\nu_0 r_{ij} \cdot \nabla_i W_{ij}}{(\rho_i + \rho_j)(r_{ij}^2 + \eta^2)} \right) v_{ij} \tag{5}$$

where  $\nu_0$  is the kinematic viscosity and  $\eta^2 = 0.01h^2$ , which is a small number introduced to maintain a nonzero denominator. Equation (4) is the general SPH form of mass conservation while Equation (5) is the expression of momentum conservation for the Laminar viscosity model.

*2.3. Computation of the Pressure Field*

In the SPH approximation, the fluid is treated as weakly compressible, and an equation of state is used to determine fluid pressure according to the particle density. The pressure field is computed using Tait’s equation of state:

$$P = B \left[ \left( \frac{\rho}{\rho_0} \right)^\gamma - 1 \right] \tag{6}$$

In Equation (6),  $B = \frac{c_s^2 \rho_0}{\gamma}$ ,  $\rho_0$  is the reference density;  $c_s$  is the speed of sound, which should be at least ten times faster than the maximum fluid velocity in order to prevent major deviations from an incompressible approach [29]; and  $\gamma = 7$ .

#### 2.4. SPH Treatment of Viscosity

The DualSPHysics code provides two viscosity treatment models. “Artificial viscosity” and “Laminar + SPS.” In this work, both models were tested and delivered with almost identical results regarding the 2D cases. However, for the 3D cases, the “Laminar + SPS” model provided better quantitative results and, therefore, it has been incorporated for all cases simulated here. It should be emphasized that the flows discussed in this work are laminar and, consequently, the sub-particle scale stress is negligible and the momentum equation takes the form of Equation (5).

#### 2.5. Kernel Function

As mentioned in Section 2.1, a kernel function,  $W$ , is used in SPH function approximation. Furthermore, a characteristic cut-off length,  $h$ , is selected. The physical property of any particle is calculated by the summation of the relevant properties of all neighboring particles within the selected range. In this study, the quintic Wendland function is used as kernel defined as

$$W(r, h) = \alpha_D \left(1 - \frac{q}{2}\right)^4 (2q + 1) \quad 0 \leq q \leq 2 \tag{7}$$

where  $q$  is the nondimensional distance between particles,  $\alpha_D = 7 / (4\pi h^2)$  for 2D simulations, and  $\alpha_D = 21 / (16\pi h^3)$  in 3D.

#### 2.6. Integration in Time

In the weakly compressible formulation of SPH the governing partial differential equations (PDEs), Equations (1) and (2) are transformed into a set of ordinary differential equations (ODEs), namely Equations (4) and (5). For a representative particle  $\alpha$ , the ODEs are written symbolically in the form

$$\frac{d\rho_\alpha}{dt} = R_\alpha; \quad \frac{dV_\alpha}{dt} = F_\alpha; \quad \frac{dr_\alpha}{dt} = V_\alpha; \tag{8}$$

where an ODE is added for the particle position,  $r_\alpha$ .

The formulae in Equation (8) are integrated in time using the symplectic position or Verlet algorithm. The timestep,  $\Delta t$ , is limited by Courant–Friedrichs–Lewy (CFL) conditions because of the underlying PDEs. Furthermore, the time step depends on the forcing term,  $F_\alpha$ , and the viscous diffusion term. Specifically, the timestep satisfies the relations

$$\Delta t = CFL \min(\Delta t_f, \Delta t_{cv}) \tag{9}$$

where

$$\Delta t_f = \min_\alpha \left( \sqrt{\frac{h}{|f_\alpha|}} \right) \text{ and} \tag{10}$$

$$\Delta t_{cv} = \min_\alpha \left( \frac{h}{c_s + \max_b \left| \frac{h v_b \cdot r_a}{r_{ab}^2 + \eta^2} \right|} \right) \tag{11}$$

In Equation (11),  $c_s$  denotes the speed of sound and  $|f_\alpha|$  is the force per unit mass.

### 3. Results

#### 3.1. Two-Dimensional Flows

The first group of simulations includes four cases of water flow through closed 2D microchannels. The nominal water density is assumed equal to 1000 kg/m<sup>3</sup>. In simulations using DualSPHysics code, the liquid is considered weakly compressible [29]. Small deviations of the water density (of the order of 0.1%) are observed locally. The parameters of the baseline simulations, the BCs, as well as the computational time that is needed on a GPU RTX 3060 card are summarized in Table 1. Here, DBC stands for dynamic boundary conditions,  $N_p$  denotes the number of fluid particles,  $dp$  is the initial interparticle distance, and  $\nu_0$  the kinematic viscosity.

**Table 1.** Model parameters of 2D baseline simulations.

Case	Poiseuille	Developing Flow	Sudden Expansion	Expansion/Contraction
$N_p$	10,000	10,060	10,340	15,300
$dp$ (m)	$2.00 \times 10^{-5}$	$2.00 \times 10^{-5}$	$2.98 \times 10^{-5}$	$2.98 \times 10^{-5}$
$\nu_0$ (m <sup>2</sup> /s)	$1.00 \times 10^{-6}$	$1.00 \times 10^{-6}$	$1.00 \times 10^{-6}$	$1.00 \times 10^{-6}$
BCs at solid wall	DBC	DBC	DBC	DBC
BCs in x-direction	Periodic	Inlet/outlet	Inlet/outlet	Periodic
Force per unit mass (m/s <sup>2</sup> )	$g_x = 0.001$	$g_x = 0.0$	$g_x = 0.0$	$g_x = 0.001$
Time Integration	Verlet	Verlet	Symplectic	Symplectic
Simulation time (s)	5	5	20	30
GPU time (min)	2.1	2.5	10	8

##### 3.1.1. Constant Cross Section Microchannel

###### Fully Developed Flow Model

In the first preliminary test case, the fluid is confined between two very large parallel solid plates (Figure 1a). The gap between the plates is  $H = 2h = 0.985$  mm. Periodic boundary conditions (PBCs) are applied in streamwise (x-axis) and in spanwise (z-axis) (Figure 1b). This computational setup corresponds to the well-known Poiseuille flow. Zero velocity is applied at  $t = 0$  everywhere in the flow field in the baseline simulation. After a certain simulation time, the flow reaches steady conditions. In further simulations, the same solution is reached independently of the initial flow conditions considered.

The x-velocity component, computed using the SPH method, is compared to the analytical velocity profile in Figure 2. For easy reference, we provide the analytical solution to the N–S equations for laminar Poiseuille flow here [30]. The exact velocity field is

$$u = -\frac{Gh^2}{2\mu} \left( 1 - \frac{y^2}{h^2} \right), v = 0, w = 0 \tag{12}$$

where the y-axis is in the wall–normal direction,  $\mu$  is the dynamic viscosity of the fluid, and  $2h$  is the gap between the two plates. Equation (12) is valid for a coordinate system with the x-axis in the mid-plane of the configuration. The driving pressure gradient is denoted by  $G = \frac{\partial P}{\partial x}$  and is a negative constant. It is noted that, instead of a pressure gradient, one can, equivalently, apply a body force of  $\rho g_x$  to drive the flow (see Table 1). For values up to  $g_x = 0.1$  m/s<sup>2</sup>, the velocity profile is in very good agreement with the analytical solution and the linear behavior is obvious. Values greater than 0.1 m/s<sup>2</sup> have not been tested.

The size of the gap between the two parallel plates as well as the bulk velocity of the water are small and, consequently, in all simulations, the flow Reynolds number is low [30]. As a result, the nonlinear terms of the N–S equations are negligible. The linear response of the flow is verified by doubling the driving force per unit mass using a number of numerical experiments.

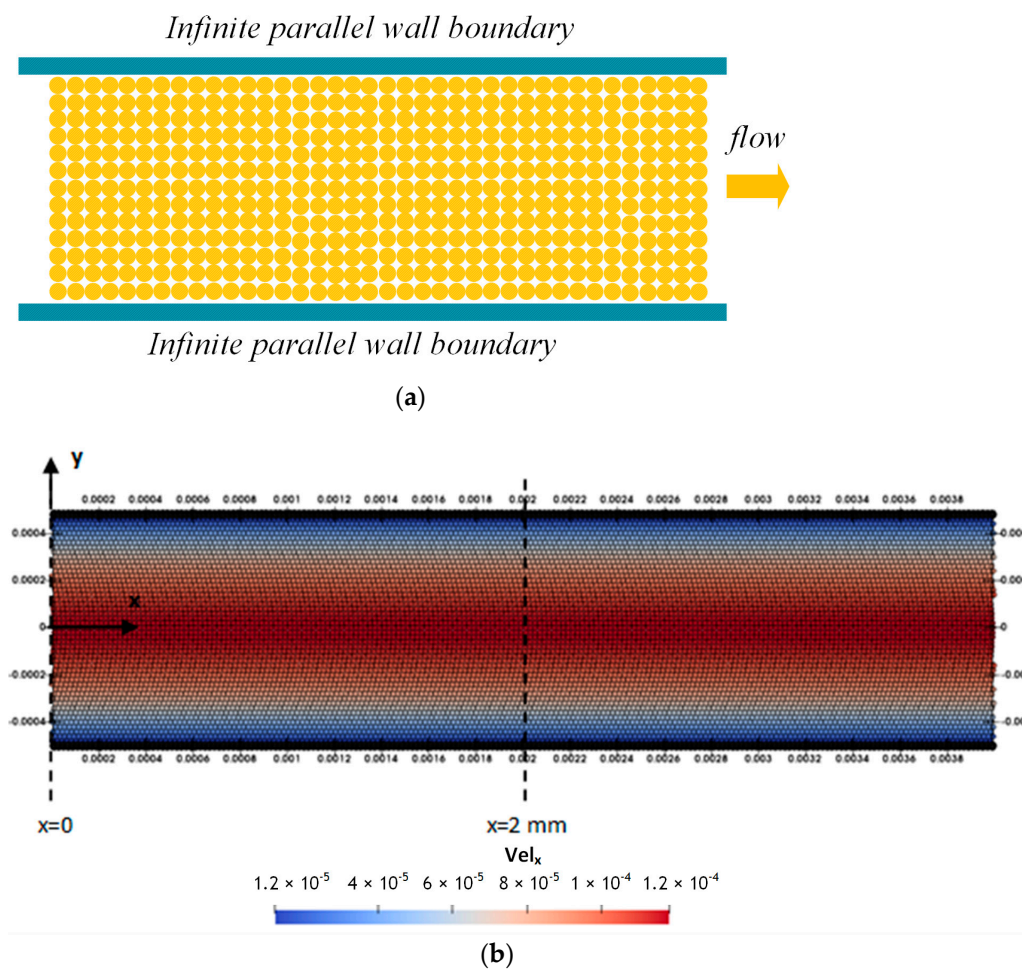


**Figure 1.** (a) Longitudinal illustration of the Poiseuille case. (b) Two-dimensional constant cross section channel. Geometry and coordinate system in 2D simulations.

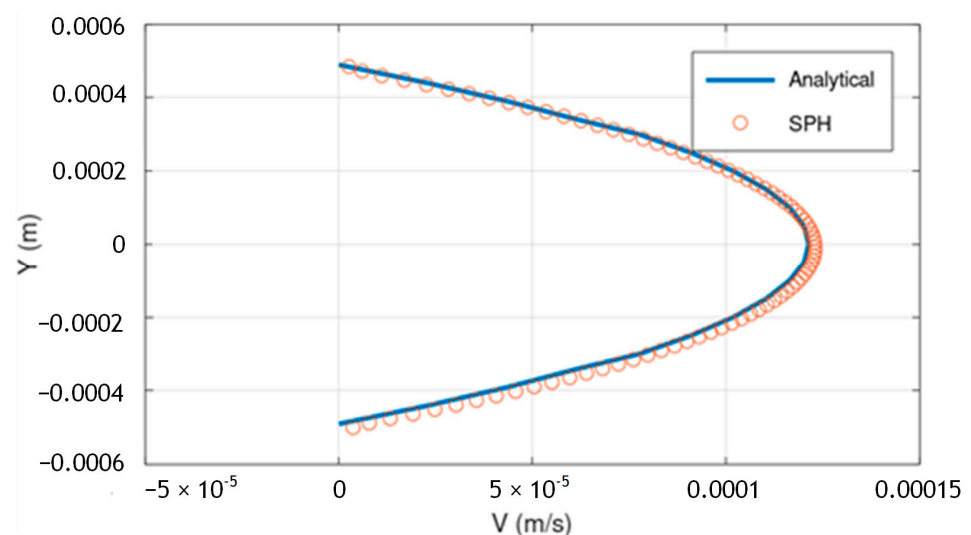


**Figure 2.** Poiseuille flow. Computed velocity profile at  $x = 2 \text{ mm}$ . Comparison with the analytical profile (Equation (12)).

### Wall Shear Stress and Friction Factor

The shear stress at the solid walls of channels is of great practical importance across all scales: nano, micro, and macro [31], since it is directly related to the pressure drop along

the channel and, consequently, to the power required for fluid transport. For a Newtonian fluid, the wall shear stress is calculated as

$$\tau_w = \mu \left. \frac{du}{dy} \right|_{wall} \tag{13}$$

and, for the coordinate system described in the context of Equation (12),  $|\tau_w| = |G|h = \mu u_{max} \frac{2}{h}$ . In Table 2, we summarize the comparison between the computed velocity derivative at the wall in the baseline simulation and its exact analytical value, and the relative difference obtained is 2.04% for both boundary conditions. By increasing the driving force per unit mass, we further simulated Poiseuille flow at different values of the Reynolds number. In Figure 3, we present the relation between the friction factor,  $f$ , and the flow Reynolds number as predicted by the SPH simulation. The definitions adopted here are

$$f = \frac{\tau_w}{\frac{1}{8}\rho\bar{V}^2} = \frac{\left(-\frac{\partial p}{\partial x}\right)D_h}{\rho\frac{\bar{V}^2}{2}}, \quad Re = \frac{\bar{V}D_h}{\nu_0}, \quad D_h = \frac{4A}{P} = 2H = 4h, \tag{14}$$

where  $D_h$  is the hydraulic diameter and  $V$  is the mean velocity at the cross-section.

**Table 2.** Two-dimensional constant cross-section channel. Comparison between SPH results with analytical solution for the derivative of x-velocity component.

Baseline Simulation	SPH	Analytical	Rel. Diff. (%)
Periodic BCs	0.48	0.49	2.04%
Inlet/outlet BC with buffer zones	0.48	0.49	2.04%

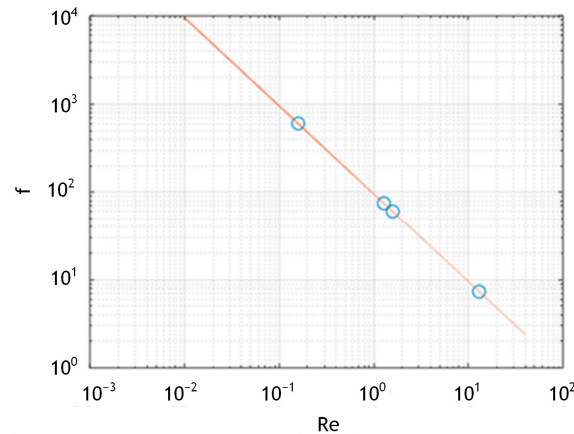


**Figure 3.** Two-dimensional Poiseuille flow. Least square fit of the  $f$  vs.  $Re$  relation based on SPH simulations.

The least squares fit of the computed values of the friction factor delivers  $f = 95.9/Re$  (see Figure 3), which is in excellent agreement with the exact value of the Poiseuille number,  $Po = f \times Re = 96 = \text{const.}$  [30].

### Developing Flow Model

Next, we studied the developing laminar flow in the gap between two very large parallel plates. Since the developing length of the flow is not known a priori, PBCs in the  $x$ -direction are not appropriate and they are replaced by inlet/outlet BCs. In this formulation, two buffer zones are constructed at the pre-processing step. Uniform-in-space and constant-in-time velocity and pressure, respectively, are applied at the inlet buffer zone. These buffer zones interact with the fluid particles using ghost nodes, passing all the information to fluid particles at the inflow and outflow [29]. In the baseline simulation,

the uniform velocity at the inlet is set equal to  $8.075 \times 10^{-5}$  m/s. The initial conditions correspond to water in equilibrium. After the flow reaches fully developed flow conditions, the fully developed SPH results are in excellent agreement with the exact solution of the fully developed Poiseuille flow (see Figure 4a).

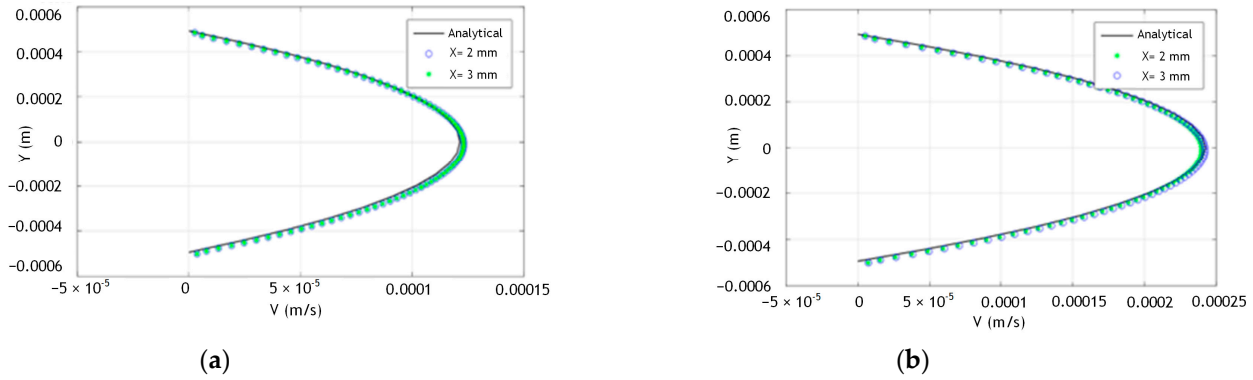


**Figure 4.** Developing flow model. Computed velocity profile at  $x = 2$  mm and  $x = 3$  mm. Comparison with the analytical profile (Equation (12)). (a)  $V_{inlet} = 8.075 \times 10^{-5}$  m/s. (b)  $V_{inlet} = 1.605 \times 10^{-4}$  m/s.

To assess the model’s behavior regarding the increase in flowrate, we doubled the magnitude of the inlet velocity. The maximum velocity, mean velocity, and, consequently, flowrate and Reynolds number doubled. The fully developed SPH results show excellent agreement with the analytical Poiseuille profile (see Figure 4b).

3.1.2. Two-Dimensional Sudden Expansion

In this numerical experiment, a sudden increase in the linear dimensions of the channel cross-section is introduced. The distance between the two solid walls increases suddenly from 0.4925 mm to 0.985 mm at  $x = 4$  mm. The geometry of the channel and the length of each portion of the channel are shown in Figure 5. Boundary conditions in the streamwise direction are applied using an inlet buffer zone with constant-in-time and uniform-in-space velocity and free outflow conditions at the outlet of the computational domain (see Figure 5). The inlet velocity is set equal to  $3.125 \times 10^{-5}$  m/s, while the initial velocity conditions are set equal to zero  $u = v = w = 0$  everywhere in the flow field.

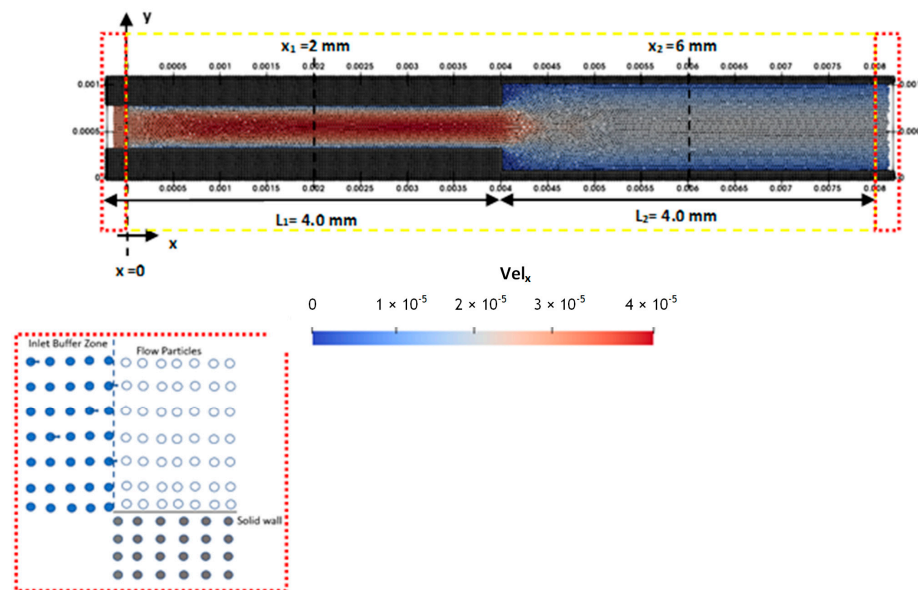


**Figure 5.** Two-dimensional sudden expansion. Overall geometry and computational domain. Flow field snapshot at  $t = 20$  s.

Figures 5 and 6 show the particles and the trajectory lines at  $t = 20$  s when the flow reaches steady flow conditions. Well-defined vortices are formed immediately after the channel’s sudden expansion. Although the Reynolds number is small, the flow separates because of the sharp  $90^\circ$  corner and reattaches after a length slightly larger than the “step” height (see Figure 6).

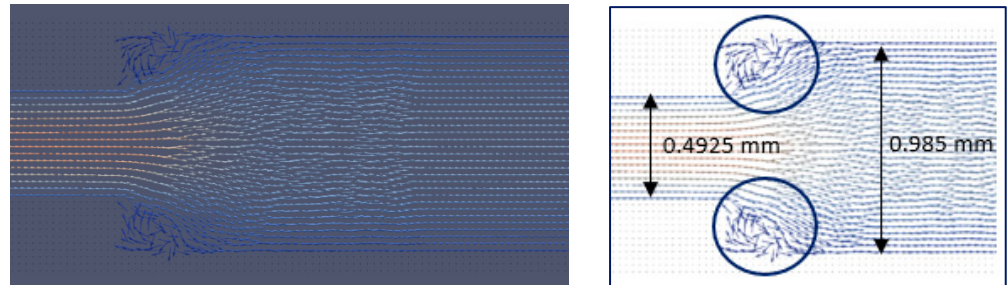


**Figure 6.** Two-dimensional sudden expansion. Flow field snapshot and trajectory lines at  $t = 20$  s. Arrows demonstrate velocity direction and are colored by velocity values (not scaled).

Velocity profiles in two different longitudinal positions (Figure 7) exhibit the expected parabolic behavior with the max velocity values to be located at the center of the closed channel and velocity values tend to zero, close to the boundary (solid–fluid interface). Some inaccuracies occurred, mainly due to the treatment of fluid–solid interface BCs since strict no-slip conditions have not been implemented yet in the DualSPHysics version used for this study [29]. Inaccuracies are more apparent in the narrower cross-section. This is mainly due to the separation distance between the plates in combination with the larger velocity.

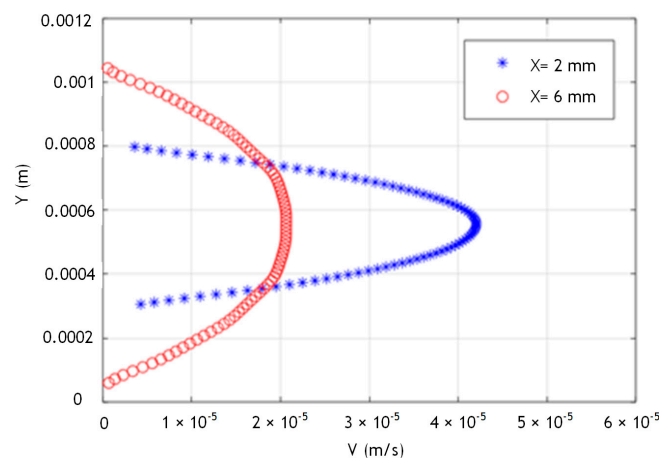


**Figure 7.** Two-dimensional sudden expansion. Velocity profiles at longitudinal positions  $x_1 = 4$  mm,  $x_2 = 6$  mm. At  $x_1$ ,  $\bar{V}_1 = 2.89 \times 10^{-5}$  m/s, ( $Q_1 = 1.42 \times 10^{-11}$  m<sup>3</sup>/s), while at  $x_2$ ,  $\bar{V}_2 = 1.43 \times 10^{-5}$  m/s, ( $Q_2 = 1.41 \times 10^{-11}$  m<sup>3</sup>/s) (rel. difference 0.7%).

### 3.1.3. Two-Dimensional Sudden Expansion/Contraction

In the last 2D case considered, the distance between the solid walls increases suddenly at  $x = 0$  from 0.4925 mm to 0.985 mm and decreases suddenly at  $x = 3.6$  mm back to 0.4925 mm (see Figure 8). The aim, in this case, is to model the flow in a very long channel with periodic expansions and contractions. The SPH model described in this subsection solves the Navier–Stokes equation in a single module of the channel as shown in Figure 8. Periodic BCs are imposed in the streamwise direction, and the initial velocity field is set equal to zero. The flow reaches a steady state after a certain time.

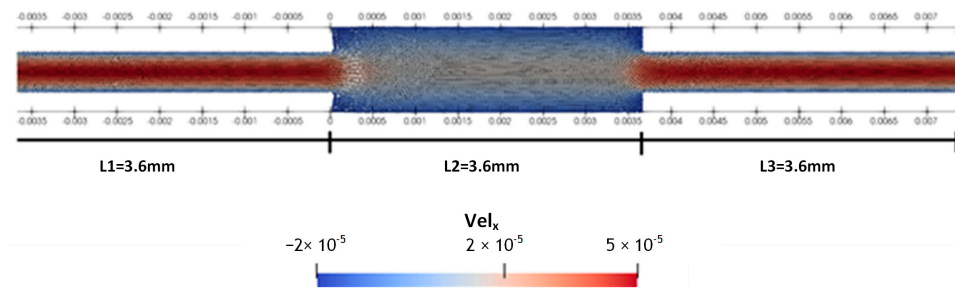


**Figure 8.** Two-dimensional sudden expansion/contraction. Overall geometry and dimensions of computational domain. Flow field snapshot at  $t = 30$  s.

An expanded view of the streamline/pathline (trajectories) pattern in the central part of computational domain is shown in Figure 9. SPH successfully captures the streamline curvature and the formation of the vortices near the corners.



**Figure 9.** Two-dimensional sudden expansion/contraction. Trajectory lines (not scaled) in the expanded section of the channel at  $t = 30$  s.

The computed velocity profiles exhibit the expected parabolic behavior at cross sections located far from the sudden expansions and contractions. In Figure 10, the velocity profiles at longitudinal positions  $x_1 = -2$  mm,  $x_2 = 2$  mm, and  $x_3 = 6$  mm are shown. Corresponding cross-sectional average velocities are  $\bar{V}_1 = 1.5 \times 10^{-5}$  m/s =  $\bar{V}_3$ ,  $\bar{V}_2 = 3 \times 10^{-5}$  m/s, and  $Q_1 = Q_2 = Q_3 = 7.38 \times 10^{-12}$  (m<sup>3</sup>/s) =  $7.38 \times 10^{-2}$   $\mu$ L/s.

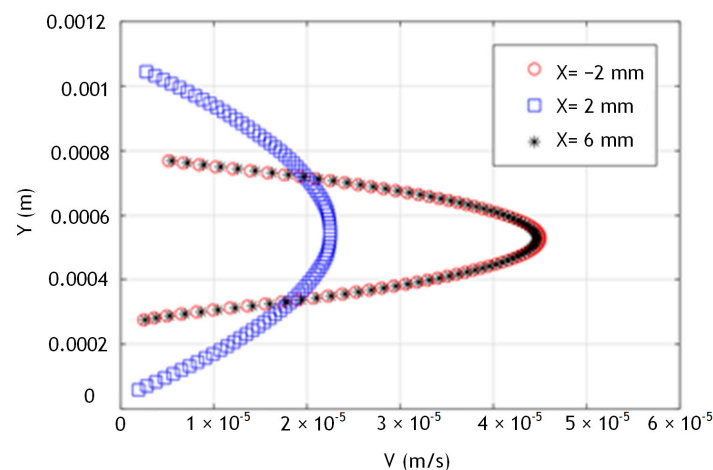


**Figure 10.** Two-dimensional sudden expansion/contraction. Velocity profiles at longitudinal positions  $x_1 = -2$  mm,  $x_2 = 2$  mm, and  $x_3 = 6$  mm. Corresponding cross-sectional average (mean) velocities  $\bar{V}_1 = 1.5 \times 10^{-5}$  m/s =  $\bar{V}_3$ ,  $\bar{V}_2 = 3 \times 10^{-5}$  m/s, and volume flowrates are  $Q_1 = Q_2 = Q_3 = 7.38 \times 10^{-12}$  (m<sup>3</sup>/s) =  $7.38 \times 10^{-2}$   $\mu$ L/s.

The conservation of mass principle is perfectly satisfied. This implies that there is no leakage of fluid particles through the walls of the channel, a typical difficulty in purely particle numerical methods.

### 3.2. Three-Dimensional Flows

In this section, we present results of SPH simulations of flows in straight microducts of a square cross-section. Transverse and longitudinal sections of the microchannels studied are presented in Figure 11. We bring to the attention of the reader that, in the 3D SPH simulations, the x-axis lies in the lower wall and the z-axis is chosen in the direction normal to the upper and lower walls. The y-axis is in the spanwise direction. Physical and computational parameters, BCs, and the methods of integration-in-time used in the baseline simulations are listed in Table 3.

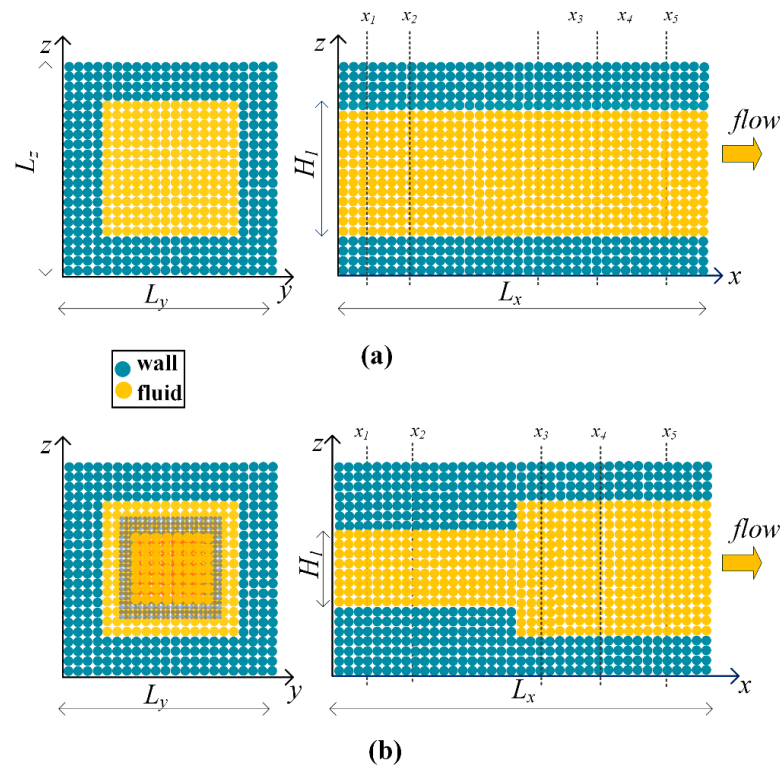


**Figure 11.** Transverse and longitudinal sections of the 3D channel model and coordinate system used in 3D SPH simulations. (a) Constant cross-section, (b) with sudden expansion of cross section.

**Table 3.** Parameters of 3D baseline simulations.

Case	Const. C.S. (A)	Const. C.S. (B)	Sudden Expansion	Expan./Contr.
Np	216,480	308,788	581,040	897,334
dp (m)	$2.98 \times 10^{-5}$	$2.98 \times 10^{-5}$	$2.98 \times 10^{-5}$	$2.98 \times 10^{-5}$
$\nu_0$ (m <sup>2</sup> /s)	$1.00 \times 10^{-6}$	$1.00 \times 10^{-6}$	$1.00 \times 10^{-6}$	$1.00 \times 10^{-6}$
BCs at solid walls	DBC	DBC	DBC	DBC
BCs in x-direction	Periodic	Inlet/outlet	Inlet/outlet	Periodic
Force per unit mass (m/s <sup>2</sup> )	$g_x = 0.001$	$g_x = 0.0$	$g_x = 0.0$	$g_x = 0.001$
Time integration	Symplectic	Symplectic	Symplectic	Symplectic
T (s)	20	50	60	50
GPU time (min)	13.6	24.6	38.85	51

#### 3.2.1. Fully Developed Flow in a Square Duct of Constant Cross-Sectional Area

The first 3D case considered consists of a constant cross-section long microchannel with  $L_y = L_z = 1.104$  mm (see Figure 11a). The fluid occupies a net area of  $0.985$  mm  $\times$   $0.985$  mm while the length of the computational domain in the x-direction is set equal to  $3.6$  mm. The flow is considered fully developed so that periodic BCs are applied in the x-direction. DBCs are imposed on solid walls. A number of initial conditions for the velocity field were tested (zero, uniform in space, etc.), complying with the conservation of mass principle.

The magnitude of the streamwise velocity component (obtained using SPH) is shown in Figure 12 using a color-coded plot.

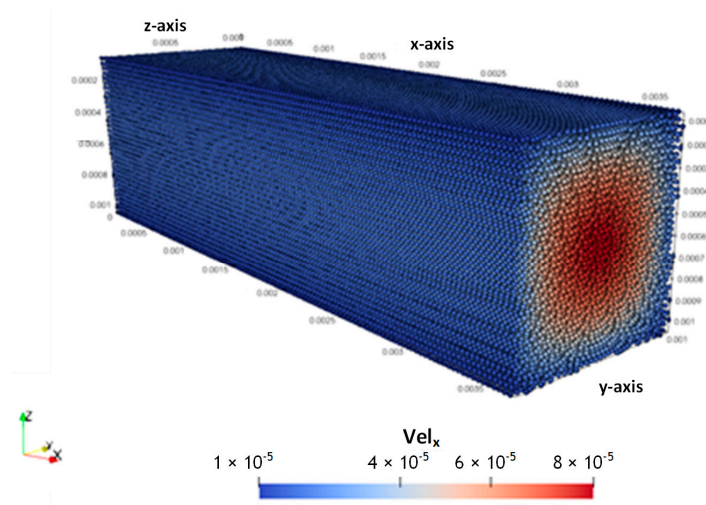


**Figure 12.** Three-dimensional constant cross-section channel. PBCs. x-velocity component (steady flow,  $t = 20$  s).

An exact infinite series solution of laminar flow in a straight channel of a rectangular cross-section can be found in the literature [32]. Specifically, the velocity field and the volume flowrate are

$$u(y, z) = \frac{16a^2}{\mu\pi^3} \left( -\frac{\partial P}{\partial x} \right) \sum_{i=1,3,5..}^{\infty} (-1)^{(i-1)/2} \left[ 1 - \frac{\cosh(i\pi z/2a)}{\cosh(i\pi b/2a)} \right] \times \frac{\cos\left(\frac{i\pi y}{2a}\right)}{i^3} \quad (15a)$$

$$Q = \frac{4b\alpha^3}{3\mu} \left( -\frac{\partial P}{\partial x} \right) \left[ 1 - \frac{192a}{\pi^5 b} \sum_{i=1,3,5..}^{\infty} \frac{\tanh\left(\frac{i\pi b}{2a}\right)}{i^5} \right] \quad (15b)$$

In Equations (15a) and (15b),  $\alpha$  and  $b$  represent the half lengths of the rectangular cross section along the y-axis and z-axis, respectively. In the cases presented in this work,  $\alpha = b$ . Note that, in Equation (15a), the x-axis is chosen along the axis of symmetry of the duct.

The SPH numerical solution and the analytical solution are compared in terms of the x-velocity distribution in Figure 13 and velocity profiles in Figure 14. The agreement between them is very good.

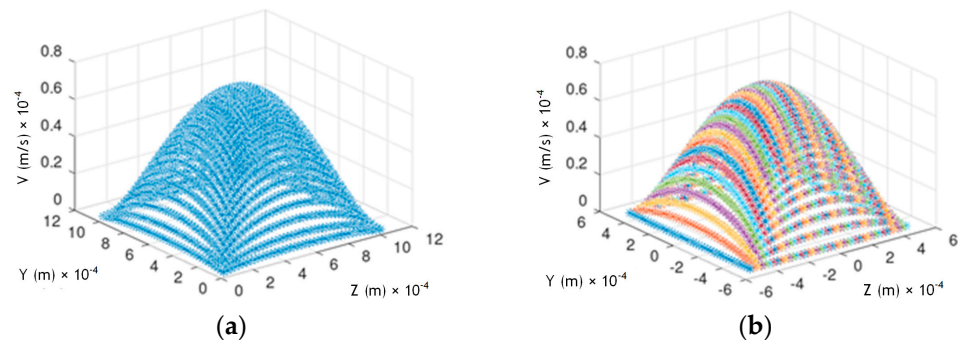


**Figure 13.** Three-dimensional constant cross-section microchannel. Periodic BCs. x-velocity component distribution  $u(Y, Z)$ : (a) SPH-computed profile at  $x = 2$  mm and (b) analytical solution (Equation (15a)).

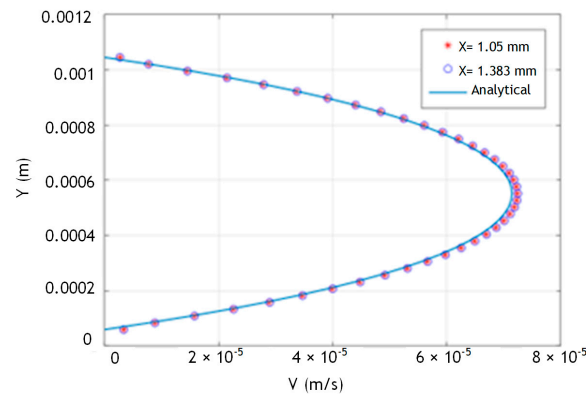


**Figure 14.** Three-dimensional constant cross-section channel. Periodic BCs. SPH velocity profile  $u(Z, Y = 0.4925 \text{ mm})$  at  $x = 1.05 \text{ mm}$  and  $x = 1.383 \text{ mm}$  and analytical solution velocity profile  $u(z, y = 0)$ , where  $z = Z - 0.4925 \times 10^{-3}(\text{m})$ ,  $y = Y - 0.4925 \times 10^{-3}(\text{m})$ .

The computed volume flowrate (discharge) is close to the analytical value, Equation (15b), with a relative error of 3%. This level of accuracy is obtained with the computational parameters listed in Table 3 in the column designated as constant C.S. (A). Increasing the number of particles in the simulation decreases the relative error as long as associated parameters are adjusted appropriately.

Poiseuille Number, the Relation  $f$  vs.  $Re$

For the design of microdevices, energy loss can be calculated using the relation  $f$  vs.  $Re$ . By changing the driving force per unit mass, we simulated the flow at various values of the Reynolds number. In Figure 15, we present the relation between the friction factor  $f$  and the Reynolds number based on cross-sectional average velocity and hydraulic diameter  $D_h$ . In the case of a square duct, the hydraulic diameter  $D_h$  is equal to the square side length.

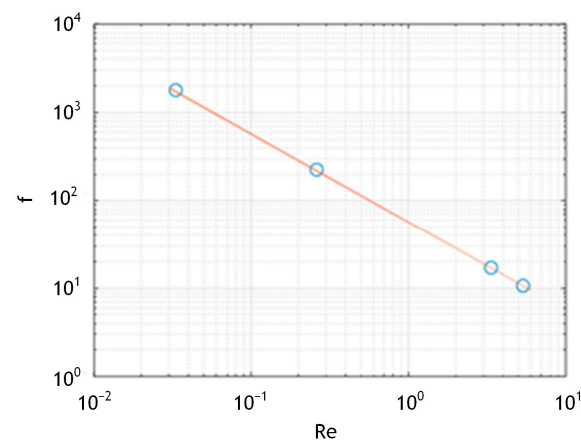


**Figure 15.** Three-dimensional constant cross-section. Periodic BCs. Least square fit of the  $f$  vs.  $Re$  relation based on SPH simulations.

Least squares fit of the computed data provides the correlation  $f = 57.4/Re$  (see Figure 15), which is in very good agreement with the exact value for the Poiseuille number for the square duct,  $Po = f \times Re = 56.9 = \text{const.}$  [30].

3.2.2. Developing Flow in a Square Microduct of Constant Cross-Sectional Area

To assess the SPH performance in simulating 3D developing flow, we replaced the PBCs with inlet/outlet buffer zones. As the inlet condition, we applied constant-in-time and uniform-in-space velocity distribution,  $V_{\text{inlet}} = 3.4 \times 10^{-5} \text{ m/s}$ .

The flow reaches steady state conditions after a certain time, and fully developed flow is established at approximately  $x = 1$  mm. The developing length ( $L_{dev}$ ) is very short and well within the length of the computational domain in the streamwise direction (Figure 16).

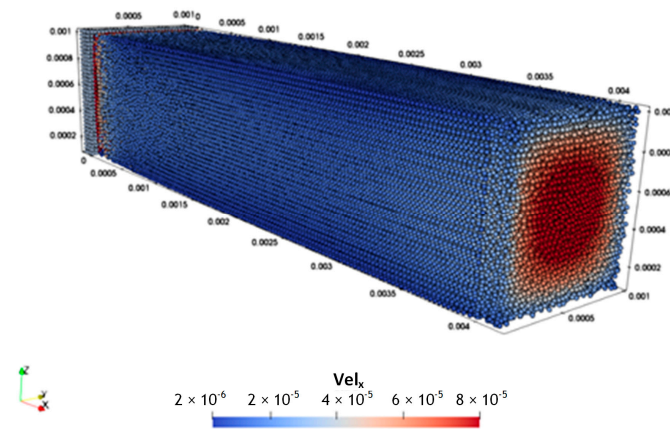


**Figure 16.** Three-dimensional constant cross-section microchannel. Developing flow. x-velocity component (steady flow,  $t = 50$  s).

The development of the flow profile in the vertical mid-plane ( $Y = 0.4925$  mm) is shown in Figure 17 while the 3D plot of the velocity distribution at  $x = 1.05$  mm is depicted in Figure 18.

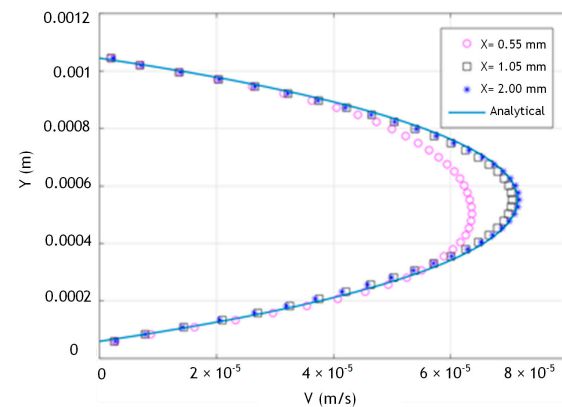


**Figure 17.** Three-dimensional constant cross-section microchannel. Developing flow. SPH-computed velocity profile development at the vertical mid-plane ( $Y = 0.4925$  mm).

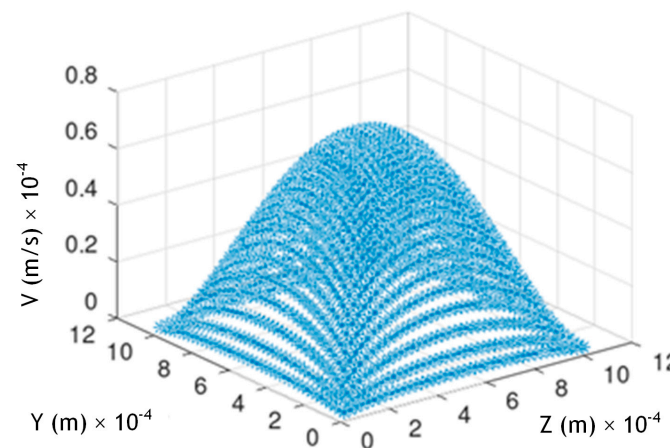


**Figure 18.** Three-dimensional constant cross-section microchannel. Developing flow. Velocity distribution  $u$  ( $Y, Z$ ) at cross-section  $x = 2$  mm in the fully developed region.

The computed mean velocity at  $x = 1.05 \text{ mm}$  equals  $\bar{V}_{\text{sph}} = 3.3 \times 10^{-5} \text{ m/s}$ , showing a relative error of 3% when compared to the analytical solution. Discharge:  $Q_{\text{SPH}} = 3.2 \times 10^{-11} \text{ m}^3/\text{s} = 3.2 \times 10^{-2} \text{ }\mu\text{L/s}$ . We note that the use of inlet/outlet BCs demanded more computational time, mainly due to the longer time that the flow needs to reach steady state conditions.

### 3.2.3. Three-Dimensional Microchannel with Sudden Expansion

In a sudden expansion, it is assumed at  $x = 4 \text{ mm}$  (see Figure 19). For  $x < x_{\text{exp}}$ , the net cross-section area that the fluid occupies is  $L_y \times L_z = 2.426 \times 10^{-7} \text{ m}^2 \approx 0.24 \text{ mm}^2$ . For  $x > x_{\text{exp}}$  the net cross section that the fluid occupies is  $L_y \times L_z = 9.702 \times 10^{-7} \text{ m}^2 \approx 0.97 \text{ mm}^2$ . For this case, there are two additional issues that need to be addressed: the selection of the inlet velocity value and the number of particle layers that form the solid boundaries (walls). To hold the fluid particles within the cross-section, we apply five layers of solid particles to form the walls. The solid particle arrangement has the same interparticle distance as that of the initial fluid particle configuration.

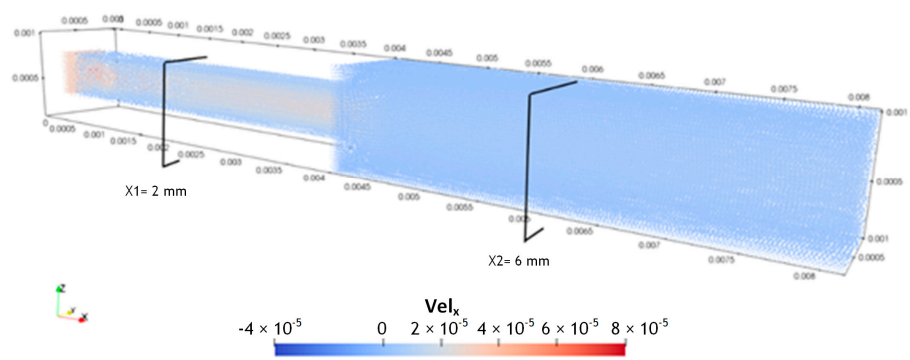


**Figure 19.** Three-dimensional sudden expansion. x-velocity component (steady flow,  $t = 60 \text{ s}$ ).

In Figure 19, only the fluid particles are presented and seem to qualitatively follow the expected flow pattern.

The mean velocity values and discharge are computed (Figure 20) and compared at two longitudinal points:  $x_1 = 2 \text{ mm}$  and  $x_2 = 6 \text{ mm}$  (Figure 21).

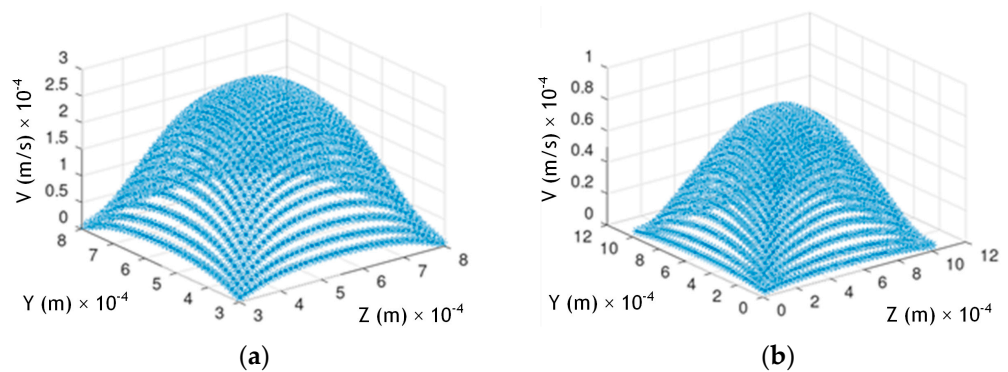


**Figure 20.** Three-dimensional sudden expansion. Velocity distribution  $u(y, z)$  (a)  $x_1 = 2 \text{ mm}$ ,  $\bar{V}_1 = 1.49 \times 10^{-5} \text{ m/s}$ ,  $Q_1 = (0.4925)^2 \times 10^{-6} \times \bar{V}_1 = 3.61 \times 10^{-12} \text{ m}^3/\text{s}$ ; and (b)  $x_2 = 6 \text{ mm}$ ,  $\bar{V}_2 = 3.72 \times 10^{-6} \text{ m/s}$ ,  $Q_2 = 3.61 \times 10^{-12} \text{ m}^3/\text{s}$ . Relative difference 0%.

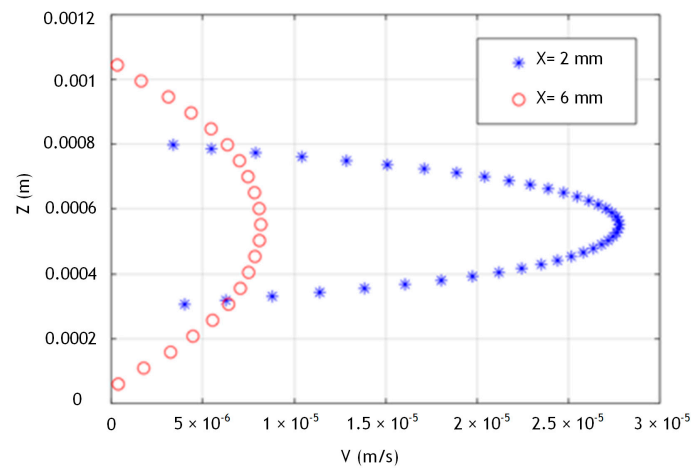


**Figure 21.** Three-dimensional sudden expansion. Velocity profile  $u(z, y = 0.4925 \text{ mm})$ ,  $x_1 = 2 \text{ mm}$ ,  $x_2 = 6 \text{ mm}$ .

### 3.2.4. Three-Dimensional Microchannels with Periodic Expansions/Contractions

In the final 3D numerical experiment, we examine the flow in a very long channel (duct) characterized by periodic expansions and contractions of the cross-sectional area. Taking advantage of the microchannel’s geometry, we simulate the flow by selecting an appropriate computational domain (module) where PBCs can be imposed in the streamwise  $x$ -direction (Figure 22). The length of the module is 12 mm while the cross-section areas occupied by the fluid are  $(0.4925 \text{ mm} \times 0.4925 \text{ mm})$  and  $(0.985 \text{ mm} \times 0.985 \text{ mm})$ .

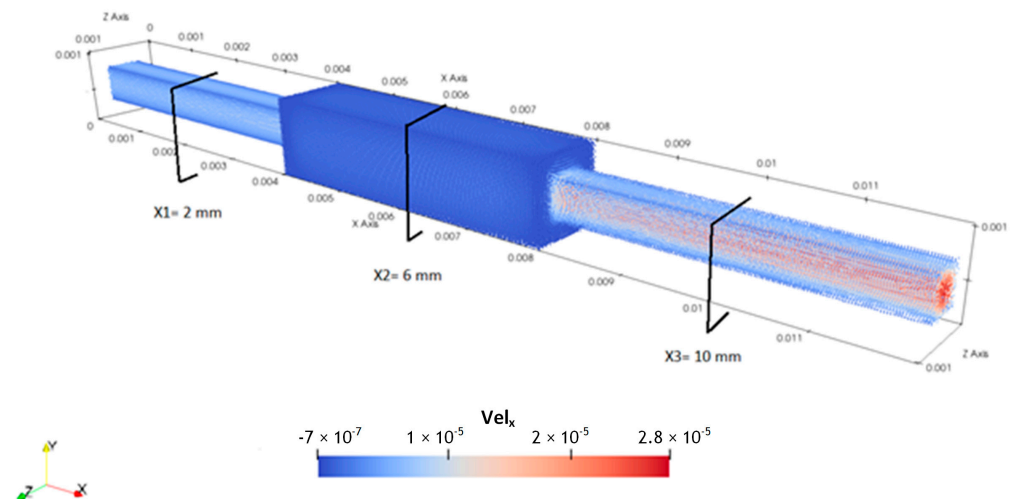


**Figure 22.** Three-dimensional microchannel with periodic sudden expansions/contractions. The computational domain is a module of the microchannel selected in such a way that periodic BCs can be applied in  $x$ -direction. Magnitude of  $x$ -velocity component (steady state,  $t = 50 \text{ s}$ ).

In the simulation, the fluid moves under the action of a body force per unit volume  $\rho g_x$ , which corresponds to a pressure gradient  $dp/dx$ . At time  $t = 0$  the fluid is considered motionless.

Since there is no analytical solution for comparison, examination of the flow field reveals qualitatively reasonable results (Figure 22). To the authors’ knowledge, there is no published numerical solution with conventional CFD methods for the problem at hand. Consequently, as a further test, we checked the degree that the SPH solution satisfies the conservation of mass (most importantly to ensure that we do not have leakage of fluid particles through the solid walls). We observed that the continuity equation is confirmed (Figure 23).

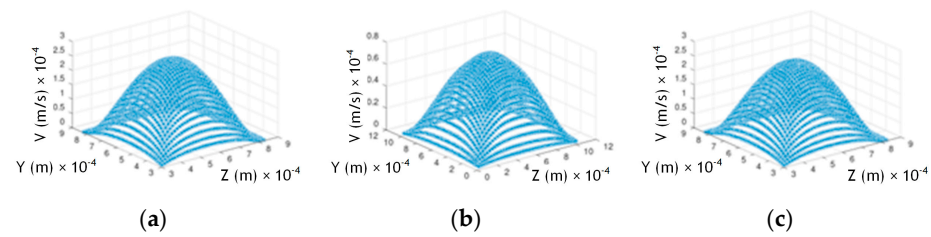


**Figure 23.** Three-dimensional microchannel with periodic sudden expansions/contractions. Velocity distribution  $u(z, y)$  for selected longitudinal positions. (a)  $x_1 = 2$  mm, (b)  $x_2 = 6$  mm, and (c)  $x_3 = 10$  mm.  $\bar{V}_1 = 1.31 \times 10^{-5}$  m/s,  $\bar{V}_2 = 3.30 \times 10^{-6}$  m/s while  $\bar{V}_3 = 1.30 \times 10^{-5}$  m/s.

As a further check on the accuracy of the SPH method, we examined the linear response of the flow to an increase in the driving force,  $g_x$ . The linearity of the response is verified as can be seen in Table 4 with the linear behavior of the volume flow rate (and the velocity, respectively) to be clearly presented in Figure 24.

**Table 4.** Mean velocity,  $\bar{V}$ , and volume flowrate,  $Q$ , at selected longitudinal stations.

x (mm)	$g_x = 0.001 \text{ m/s}^2$		$g_x = 0.002 \text{ m/s}^2$	
	$\bar{V}(\frac{\text{m}}{\text{s}}) \times 10^{-5}$	$Q(\frac{\text{m}^3}{\text{s}}) \times 10^{-11}$	$\bar{V}(\frac{\text{m}}{\text{s}}) \times 10^{-5}$	$Q(\frac{\text{m}^3}{\text{s}}) \times 10^{-11}$
2	1.31	0.32	2.6	0.63
3	1.31	0.32	2.6	0.63
6	0.33	0.32	0.66	0.64
7	0.33	0.32	0.65	0.63
10	1.30	0.32	2.58	0.63
11	1.30	0.32	2.58	0.63

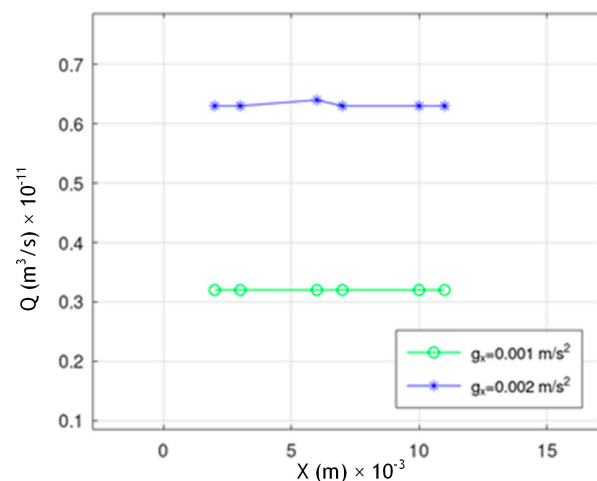


**Figure 24.** Volume flow rate plot for  $g_x = 0.001 \text{ m/s}^2$  and  $g_x = 0.002 \text{ m/s}^2$ .

#### 4. Discussion

A number of subtleties in the application of SPH method were identified in the context of the eight types of flow examined.

The approximation of the N–S equations with the SPH method is very effective as long as the particles (mass points) are distributed evenly and “islands” of empty spaces in the flow field are avoided during a simulation. This type of difficulty is less pronounced in the case of the low Reynolds number flows studied in this work, compared to the high Froude number flows with hydraulic jumps reported in previous studies [33,34]. However, even for the case of confined microflows, the effective control of the particle distribution (particle shifting) is important.

The meshless nature of SPH and the kernel truncation close to boundaries can cause difficulties in enforcing BCs [35]. Using a number of BCs (DBC, at solid/fluid interfaces, inlet/outlet, and PBC in the streamwise direction), we documented the importance of using the appropriate types of BCs in the problem formulation as well as the importance of the choice of parameter values in order to conduct accurate and efficient simulations. Our 2D and 3D cases exhibit good results, and any minor inaccuracies are attributed to some of the SPH grand challenges such as BC treatment [10].

A similar microchannel flow simulation with SPH was conducted in a previous study [36], where Poiseuille flow for 1 mm distance between the infinite plates was studied by applying the artificial flow regime. Results were in good agreement with the analytical solution. However, in our case, we conducted investigation for both 2D and 3D microchannel flows, we achieved reduced simulation times for a greater number of particles and slightly better results, regarding the velocity profiles close to the solid walls.

For the 2D cases, both periodic and inlet/outlet BCs yield satisfactory results. Steady state conditions are reached as long as the initial conditions of the velocity field (not only the velocity value, which should be selected in agreement with the study case, but also how the inlet buffer zone interacts with the fluid particles) are accurately selected, and results do not violate the conservation of mass principle. We also note that this is a required post-simulation step before the quantitative analysis begins. Our numerical results show very good agreement with analytical solutions when available. Some inaccuracies occurred in the cases of the sudden expansion and expansion/contraction, and this is mainly due to the treatment of the fluid–solid interface, one of the grand challenges facing the SPH community mentioned above.

For the 3D constant cross-section cases, SPH results are in good agreement with analytical solutions both with periodic BCs (rel. error 3%) and inlet/outlet BCs (rel. error 3%) in terms of flowrate. This difference may be attributed to the treatment of solid–fluid boundaries and possibly irregular particle displacement. It should be noted that the relation  $f$  vs.  $Re$  is predicted with higher accuracy due to the one-dimensional nature of the correlation.

Based on our experience with the DualSPHysics simulation of 3D closed channels, we suggest four to five layers of solid particles to form the channel walls in the geometry specification. This precludes the possibility of wall permeability and can alleviate potential errors due to fluid particles escaping the solid boundary. In addition, it helps in the correct imposition of the boundary condition at fluid/solid interfaces.

With respect to future challenges facing the SPH method, we believe that there are two major issues: turbulence modelling and adaptivity. There is still considerable need for an accurate and robust turbulence model, especially for the simulation of fluid transport through confined channels. The model should be accurate very close to solid–fluid interfaces where boundary layers are formed at high Reynolds numbers [37]. The other major challenge in SPH research is the development of adaptive methods [10,38] in order to reduce the overall execution times.

## 5. Conclusions

Smoothed particle hydrodynamics (SPH) simulations of 2D and 3D flows in closed microchannels were carried out using the “Laminar + SPS viscosity treatment model” of the DualSPHysics code. Two different BCs in the streamwise flow direction (periodic, when applicable, and inlet/outlet BCs with buffer zones) were evaluated. It should be noted that considerable density variations appear in the fluid at the immediate vicinity of the inlet buffer zone. However, this only occurs locally between the inlet buffer zone and the fluid interface and does not “contaminate” the overall flow field. In other words, it does not extend along the  $x$ -axis. In all cases, the flow Reynolds number is small. SPH simulations captured the main flow characteristics accurately. Minor inaccuracies were observed close to the solid walls, in agreement with the findings of other SPH researchers.

Our findings suggest that inlet/outlet BCs with buffer zones work well. More generally, the careful implementation of BCs in the streamwise direction plays an important role in formulating SPH models of internal flows. In developing flows, the fully developed sections are in good agreement with the PBCs simulations.

Regarding the 2D numerical experiments, we reached the following conclusions: For the constant cross-section channels, the computed velocity profiles and analytical solution were almost identical. In addition, the computed wall shear stress shows very good agreement with the analytical N–S solution. The computed relation  $f$  vs.  $Re$  is in excellent agreement with exact results found in the fluid mechanics literature. In the case of abrupt expansion, flow separation is predicted, and vortices are clearly observed at the corners, as expected. The same holds for the sudden expansion/contraction case. Regardless of the selection of periodic or inlet/outlet BCs, all simulation models turned out to be accurate.

The 3D numerical experiments produced results that are in good agreement with analytical solutions or benchmark numerical solutions obtained with conventional CFD methods. Both test cases for the constant 3D ducts showed very good agreement with the analytical solution in terms of velocity, volume flowrate, and prediction of Poiseuille number. In the sudden expansion and expansion/contraction cases, computed volume flowrates at selected longitudinal stations satisfied the conservation of mass principle.

**Author Contributions:** Conceptualization, A.L.; Software, E.C.; Validation, A.L.; Investigation, E.C.; Resources, F.S.; Writing—original draft, E.C.; Writing—review & editing, A.L. and F.S.; Visualization, E.C., A.L. and F.S.; Supervision, A.L.; Funding acquisition, A.L. All authors have read and agreed to the published version of the manuscript.

**Funding:** This research project was supported by the Hellenic Foundation for Research and Innovation (H.F.R.I.) under the “2nd Call for H.F.R.I. Research Projects to support Faculty Members & Researchers” (Project Number: 4584). E. Chatzoglou was supported by a doctoral candidate scholarship of the Center of Research Innovation and Excellence of the University of Thessaly, funded by the Special Account for Research Grants of the University of Thessaly.

**Institutional Review Board Statement:** Not applicable.

**Informed Consent Statement:** Not applicable.

**Data Availability Statement:** Not applicable.

**Conflicts of Interest:** The authors have no conflict of interest to declare that are relevant to the content of this article.

## References

1. Groenenboom, P.; Cartwright, B.; McGuckin, D.; Amoignon, O.; Mettichi, M.; Gargouri, Y.; Kamoulakos, A. Numerical Studies and industrial applications of the hybrid SPH-fe method. *Comput. Fluids* **2019**, *184*, 40–63. [[CrossRef](#)]
2. Shadloo, M.S.; Oger, G.; Le Touzé, D. Smoothed particle hydrodynamics method for fluid flows, towards industrial applications: Motivations, current state, and challenges. *Comput. Fluids* **2016**, *136*, 11–34. [[CrossRef](#)]
3. Patino-Narino, E.A.; Idagawa, H.S.; de Lara, D.S.; Savu, R.; Moshkalev, S.A.; Ferreira, L.O. Smoothed particle hydrodynamics simulation: A tool for accurate characterization of microfluidic devices. *J. Eng. Math.* **2019**, *115*, 183–205. [[CrossRef](#)]
4. Kalteh, M.; Abbassi, A.; Saffar-Avval, M.; Harting, J. Eulerian–eulerian two-phase numerical simulation of nanofluid laminar forced convection in a microchannel. *Int. J. Heat Fluid Flow* **2011**, *32*, 107–116. [[CrossRef](#)]
5. Sofos, F.; Chatzoglou, E.; Liakopoulos, A. An assessment of SPH simulations of sudden expansion/contraction 3-D channel flows. *Comput. Part. Mech.* **2021**, *9*, 101–115. [[CrossRef](#)]
6. Zhang, Z.L.; Walayat, K.; Chang, J.Z.; Liu, M.B. Meshfree modeling of a fluid-particle two-phase flow with an improved SPH method. *Int. J. Numer. Methods Eng.* **2018**, *116*, 530–569. [[CrossRef](#)]
7. Monaghan, J.J.; Gingold, R.A. Shock simulation by the Particle Method SPH. *J. Comput. Phys.* **1983**, *52*, 374–389. [[CrossRef](#)]
8. Monaghan, J.J. Smoothed particle hydrodynamics. *Annu. Rev. Astron. Astrophys.* **1992**, *30*, 543–574. [[CrossRef](#)]
9. Nasar, A.M.A.; Fourtakas, G.; Lind, S.J.; Rogers, B.D.; Stansby, P.K.; King, J.R.C. High-order velocity and pressure wall boundary conditions in Eulerian Incompressible SPH. *J. Comput. Phys.* **2021**, *434*, 109793. [[CrossRef](#)]
10. Vacondio, R.; Altomare, C.; De Lefte, M.; Hu, X.; Le Touzé, D.; Lind, S.; Marongiu, J.-C.; Marrone, S.; Rogers, B.D.; Souto-Iglesias, A. Grand challenges for smoothed particle hydrodynamics numerical schemes. *Comput. Part. Mech.* **2020**, *8*, 575–588. [[CrossRef](#)]
11. Plimpton, S. Fast parallel algorithms for short-range molecular dynamics. *J. Comput. Phys.* **1995**, *117*, 1–19. [[CrossRef](#)]
12. Pivkin, I.V.; Caswell, B.; Karniadakis, G.E. Dissipative Particle Dynamics. *Rev. Comput. Chem.* **2010**, *27*, 85–110. [[CrossRef](#)]

13. Ellero, M.; Español, P. Everything you always wanted to know about SDPD\* (\*but were afraid to ask). *Appl. Math. Mech.* **2017**, *39*, 103–124. [[CrossRef](#)]
14. Perdikaris, P.; Grinberg, L.; Karniadakis, G.E. Multiscale modeling and simulation of Brain Blood Flow. *Phys. Fluids* **2016**, *28*, 021304. [[CrossRef](#)]
15. Albano, A.; le Guillou, E.; Danzé, A.; Moulitsas, I.; Sahputra, I.H.; Rahmat, A.; Duque-Daza, C.A.; Shang, X.; Ng, K.C.; Ariane, M.; et al. How to modify LAMMPS: From the prospective of a particle method researcher. *ChemEngineering* **2021**, *5*, 30. [[CrossRef](#)]
16. Liakopoulos, A.; Sofos, F.; Karakasidis, T.E. Darcy-Weisbach friction factor at the nanoscale: From Atomistic calculations to continuum models. *Phys. Fluids* **2017**, *29*, 052003. [[CrossRef](#)]
17. Sofos, F.; Karakasidis, T.E.; Liakopoulos, A. Fluid flow at the nanoscale: How fluid properties deviate from the bulk. *Nanosci. Nanotechnol. Lett.* **2013**, *5*, 457–460. [[CrossRef](#)]
18. Jacob, B.; Drawert, B.; Yi, T.-M.; Petzold, L. An arbitrary lagrangian eulerian smoothed particle hydrodynamics (Ale-SPH) method with a boundary volume fraction formulation for fluid-structure interaction. *Eng. Anal. Bound. Elem.* **2021**, *128*, 274–289. [[CrossRef](#)]
19. Lyu, H.-G.; Sun, P.-N. Further enhancement of the particle shifting technique: Towards better volume conservation and particle distribution in SPH simulations of violent free-surface flows. *Appl. Math. Model.* **2022**, *101*, 214–238. [[CrossRef](#)]
20. Marrone, S.; Antuono, M.; Colagrossi, A.; Colicchio, G.; Le Touzé, D.; Graziani, G.  $\Delta$ -SPH model for simulating violent impact flows. *Comput. Methods Appl. Mech. Eng.* **2011**, *200*, 1526–1542. [[CrossRef](#)]
21. Khayyer, A.; Shimizu, Y.; Gotoh, T.; Gotoh, H. Enhanced resolution of the continuity equation in explicit weakly compressible SPH simulations of incompressible free-surface fluid flows. *Appl. Math. Model.* **2023**, *116*, 84–121. [[CrossRef](#)]
22. Monaghan, J.J. Simulating free surface flows with SPH. *J. Comput. Phys.* **1994**, *110*, 399–406. [[CrossRef](#)]
23. Morris, J.P.; Fox, P.J.; Zhu, Y. Modeling low Reynolds Number Incompressible flows using SPH. *J. Comput. Phys.* **1997**, *136*, 214–226. [[CrossRef](#)]
24. Zheng, X.; Ma, Q.; Shao, S. Study on SPH viscosity term formulations. *Appl. Sci.* **2018**, *8*, 249. [[CrossRef](#)]
25. Oger, G.; Doring, M.; Alessandrini, B.; Ferrant, P. An improved SPH method: Towards higher order Convergence. *J. Comput. Phys.* **2007**, *225*, 1472–1492. [[CrossRef](#)]
26. Colagrossi, A.; Landrini, M. Numerical simulation of interfacial flows by smoothed particle hydrodynamics. *J. Comput. Phys.* **2003**, *191*, 448–475. [[CrossRef](#)]
27. Adami, S.; Hu, X.Y.; Adams, N.A. A generalized wall boundary condition for smoothed particle hydrodynamics. *J. Comput. Phys.* **2012**, *231*, 7057–7075. [[CrossRef](#)]
28. Chen, C.; Zhang, A.M.; Chen, J.Q.; Shen, Y.M. SPH simulations of water entry problems using an improved boundary treatment. *Ocean. Eng.* **2021**, *238*, 109679. [[CrossRef](#)]
29. Domínguez, J.M.; Fourtakas, G.; Altomare, C.; Canelas, R.B.; Tafuni, A.; García-Feal, O.; Martínez-Estévez, I.; Mocos, A.; Vacondio, R.; Crespo, A.J.C.; et al. DualSPHysics: From Fluid Dynamics to multiphysics problems. *Comput. Part. Mech.* **2021**, *9*, 867–895. [[CrossRef](#)]
30. Liakopoulos, A. *Fluid Mechanics*, 2nd ed.; Tziolas Publication: Athina, Greece, 2019.
31. Liakopoulos, A.; Sofos, F.; Karakasidis, T.E. Friction factor in nanochannel flows. *Microfluid. Nanofluid.* **2016**, *20*, 24. [[CrossRef](#)]
32. White, F.M. *Viscous Fluid Flow*; McGraw-Hill: New York, NY, USA, 2006.
33. Chatzoglou, E.; Liakopoulos, A. Hydraulic Jump Simulation via Smoothed Particle Hydrodynamics: A Critical Review. In Proceedings of the 39th IAHR World Congress, Granada, Spain, 19–24 June 2022.
34. Chatzoglou, E.; Liakopoulos, A. Simulation of Open Channel Flow Control by Smoothed Particle Hydrodynamics. In Proceedings of the International Conference on Protection and Restoration of the Environment XVI, Kalamata, Greece, 5–8 July 2022.
35. English, A.; Domínguez, J.M.; Vacondio, R.; Crespo, A.J.C.; Stansby, P.K.; Lind, S.J.; Chiapponi, L.; Gómez-Gesteira, M. Modified dynamic boundary conditions (MDBC) for general-purpose smoothed particle hydrodynamics (SPH): Application to tank sloshing, dam break and Fish Pass Problems. *Comput. Part. Mech.* **2021**, *9*, 1–15. [[CrossRef](#)]
36. Liu, M.B.; Liu, G.R. Meshfree particle simulation of micro channel flows with surface tension. *Comput. Mech.* **2004**, *35*, 332–341. [[CrossRef](#)]
37. Liakopoulos, A. Computation of high speed turbulent boundary-layer flows using The  $k-\epsilon$  turbulence model. *Int. J. Numer. Methods Fluids* **1985**, *5*, 81–97. [[CrossRef](#)]
38. Fourtakas, G.; Rogers, B.D. Modelling multi-phase liquid-sediment scour and resuspension induced by rapid flows using smoothed particle hydrodynamics (SPH) accelerated with a graphics processing unit (GPU). *Adv. Water Resour.* **2016**, *92*, 186–199. [[CrossRef](#)]

**Disclaimer/Publisher’s Note:** The statements, opinions and data contained in all publications are solely those of the individual author(s) and contributor(s) and not of MDPI and/or the editor(s). MDPI and/or the editor(s) disclaim responsibility for any injury to people or property resulting from any ideas, methods, instructions or products referred to in the content.